Elastic electron-neutral collision effects on cross-field electron transport

IEPC-2024-541

Presented at the 38th International Electric Propulsion Conference, Toulouse, France
June 23-28, 2024

Shigemitsu Suzuki* and Kentaro Hara†
Stanford University, Stanford, CA, 94305, USA

A 2D axial-azimuthal particle-in-cell (PIC) simulation with electron-neutral elastic collisions is developed to investigate the effect of neutral atoms on cross-field electron transport. The electron-neutral elastic collisions are modeled with Monte Carlo collision algorithm as isotropic scattering. The key hypothesis is that the neutral atom density needs to be sufficiently high so that the growth rate of kinetic instabilities, such as the electron cyclotron drift instability (ECDI), is comparable to the electron-neutral momentum transfer collision frequency. The results with various background neutral density are discussed, showing the mitigation of plasma waves due to the collisional damping.

I. Introduction

Hall effect thrusters (HETs) have been widely expanded its population among space exploration and Earth orbiting satellite applications since 1960s. Yet, one important physics phenomenon in the HETs known as cross-field electron transport has not been fully understood. Cross-field electron mobility inferred by experiments is significantly higher than the estimated value from the classical collisional transport theory in those applications. A variety of theoretical [1, 2, 3], and numerical [4, 5, 6] approaches, including fluid and kinetic models, have been investigated. Fully kinetic Particle-in-Cell (PIC) simulations are commonly used to investigate the kinetic instabilities [7, 8] and plasma wall interactions. The validity of the PIC simulation in HETs application and the importance of the plasma instability in cross-field electron transport are discussed widely in literature [6, 9]. While linear theories are useful to understand the growth rate, they do not describe the nonlinear saturation mechanisms. Hence, fully kinetic simulations are necessary to study the growth of the instability and its saturation. In particular, such kinetic simulations are useful to study the couplings of different instabilities and how instabilities might be affected by other physical processes (e.g., neutral atoms, domain size, configuration etc.)

One particular kinetic instability that the community is focusing on is the electron cyclotron drift instability (ECDI), which is a possible candidate to explain the physics of the anomalous electron transport across magnetic field lines [10, 11]. ECDI is a type of kinetic instability that stems from the electron drift in $E \times B$ direction, leading to resonance due to the electron gyromotion (cf. electron Bernstein mode). One recent literature investigated non-linear coupling of the linear instabilities such that ECDI and ion-ion two-stream instability due to doubly and triply charged ions [12]. In addition, the instability growth rate varies when considering 2D and 3D configurations. The key difference is the presence of the electron transport along the magnetic field lines. It is predicted that the ECDI growth rate can decrease in 3D configurations when $k_{\parallel} \neq 0$, where $k_{\parallel}$ is the wave number in the direction along magnetic field lines, compared to a 2D configuration, i.e., $k_{\parallel} = 0$.

Another important research topic in the HET community is the facility effect, which results in differences of thruster performance between in-space operation and ground testing facility. Major facility effects can be finite background pressure, electrical circuit effects, and back scattering of the chamber wall material. Since

---

[*] Graduate Student, Department of Aeronautics and Astronautics, shiges@stanford.edu.

[†] Assistant Professor, Department of Aeronautics and Astronautics, kenhara@stanford.edu.

a wide range of oscillations exist in the range from 1-10 kHz and 100 kHz to 1-10 MHz in HETs, the coupling and damping of those instabilities due to electron-neutral elastic collisions may be critical to understanding the facility effect and cross-field electron transport.

In this work, we investigate the effects of elastic electron-neutral collisions on cross-field electron transport. The $E \times B$ drift shift the center of the guiding center in the phase space. Thus, the distance from the guiding center stays constant while the distance from the origin to the particle can vary over the cycle of the trapping motion. When electron-neutral collision occurs, the electron is isotropically scattered and uniformly placed at the same radius from the origin when the collision takes place in the phase space. At the post-collisional state, the radius from the guiding center of the particle can be larger or smaller compared to the pre-collisional state. The scattering uniformly randomize the particle velocity with respect to the origin. Then, the trajectory of the post-collisional particle is determined by the distance from the guiding center. In other wards, the distance from the origin is conserved through the scattering event. Nonetheless, the distance from the guiding center is not conserved. This phenomenon can contribute to the cross-field electron mobility and the evaluation of the facility effect with a finite background pressure.

II. Approach

A 2D axial-azimuthal $(z - \theta)$ PIC model for HET utilized by Charoy *et al.* [6] and Hara and Tsikata [9] is further developed to take account into elastic electron-neutral collisions. The baseline configuration and PIC simulations are the same as the $z - \theta$ benchmarking.

The electron-neutral collisions are modeled using the Monte Carlo Collision (MCC) algorithm assuming a uniform neutral species in the plasma discharge, for simplicity. The momentum transfer collision frequency of an electron colliding with background neutrals can be written as

$$\nu_m = n_n k_m, \tag{1}$$

where n_n neutral number density and k_m is collision rate coefficient.

Following the drift-diffusion formula, the cross-field electron mobility $\mu_{e,x}$, classical electron mobility $\mu_\perp$, and anomalous electron mobility $\mu_{anomalous}$ can be written as,

$$\mu_{e,x} = \frac{u_{e,x}}{E_x + \frac{1}{en_e}\frac{\partial(n_e k_B T_e)}{\partial x}}, \tag{2}$$

where $u_{e,x}$ is the electron axial bulk velocity, E_x is the axial electric field, n_e is the electron density, k_B is Boltzmann constant, and T_e is the electron temperature.

III. Particle-in-cell (PIC) simulation

The PIC simulation setup is identical to the case discussed in the benchmark paper [6] except for the introduction of the electron-neutral elastic collisions using a MCC algorith (cf. null collisions). In this section, the parameters and equations are presented.

A. Simulation parameters

Numerical parameters are shown in Table 1. The domain size, grid size, and time step are all the same as the benchmarking activities.

B. Radial magnetic field

The strength of the radial magnetic field strength profile in axial direction is imposed with a Gaussian shape.

$$B(x) = a_k \exp - \frac{(x - x_{B_{max}})^2}{2\sigma_k^2} + b_k \tag{3}$$

let $k = 1$ for $x < x_{B_{max}}$ and $k = 2$ for $x > x_{B_{max}}$. The values for a_k and b_k are available in the referenced literature [6].

Table 1: Table for the parameters in the PIC simulation

Symbol	Value	Unit
L_x	2.5	cm
L_y	1.28	cm
N_x	500	
N_y	256	
$\Delta x = \Delta y$	5×10^{-5}	m
Δt	5×10^{-12}	s
$N_{macro/cell}$	75	particles per cell

C. Ionization profile

For simplicity of the model, the ionization is considered as a source term. The electron ion pairs are injected in the middle of the domain at each timestep. The electron and ion temperatures are fixed to be 10 eV and 0.5 eV respectively. The injected particle velocities are determined from a Maxwellian velocity distribution, and the electrons and the ions are introduced at the same position. The number of injected electron-ion pairs at each timestep is determined by the following equations

$$N_{ionization} = L_y \Delta t \int_0^{L_x} S(x)dx \tag{4}$$

where the $S(x)$ is the axial ionization rate profile:

$$\begin{cases} S(x) = S_0 \cos(\pi \frac{x-x_m}{x_2-x_1}) \quad \text{for } \mathrm{x_1} \leq \mathrm{x} \leq \mathrm{x_2} \\ S(x) = 0 \quad \text{for } \mathrm{x} < \mathrm{x_1} \text{ or } \mathrm{x} > \mathrm{x_2} \end{cases} \tag{5}$$

where $x_1 = 0.25$ [cm], $x_2 = 1.0$ [cm], $x_m = 0.625$ [cm], and $S_0 = 5.23 \times 10^23$ [m^{-3} s^{-1}]. The position of the injected particle is determined with random numbers.

D. Boundary condition

In the aziuthal direction, periodic boundary conditions are applied. In the axial direction, charged particles are deleted once they reach the domain boundaries, i.e., anode at $x = 0$ cm and near-field plume at $x = 2.5$ cm. In order to hold the current continuity and the neutralize the extracted ion beam correctly, the electrons are injected at the cathode plane, which is located 1 mm from the right edge of the domain in the positive axial direction. The number of the injected electrons are calculated as follows

$$\Gamma_{e,cathode} = \Gamma_{anode} = \Gamma_{e,anode} - \Gamma_{i,anode} \tag{6}$$

where $\Gamma_{e,anode}$ and $\Gamma_{i,anode}$ are the azimuthally averaged electron and ion fluxes at the anode respectively. The injected electrons are set to 10 eV. The 1 mm shift is preventing the formation of the artificial sheath at the cathode plane.

E. Electron-neutral elastic collision

Electron-neutral elastic collisions are modeled with a MCC module. The MCC algorithm is performed by looping through all the electrons and execute whether the collisions occur based on the probability. The probability is calculated as

$$p_{collision} = \nu_m \Delta t = n_n k_m \Delta t \tag{7}$$

where $k_m = 2.5 \times 10^{-13}$ is the rate coefficient of the momentum transfer collision and Δt is the time step. In this study, neutrals are uniform and stationary in the domain. While this may not be representative of the thruster operation, this approach is taken to study the effects of electron-neutral collisions on the instabilities and their nonlinear saturation mechanisms, leading to anomalous electron transport. The comparison is performed on the i-th particle with

$$\begin{cases} \text{if } p_{collision,i} \geq rand_i, & \text{collide} \\ \text{otherwise,} & \text{no collisions} \end{cases} \tag{8}$$

where $rand_i$ is a random number and generated for each particle. This process performed for the all electron macro particles in the domain. When the collision is determined to happen, the electron go through isotropic scattering event, and the electron velocity is randomize while the magnitude of the velocity is conserved. The equations to determine the post collisional velocities are

$$\begin{aligned} v_x &= g_{pre} \cos\phi, \\ v_y &= g_{pre} \sin\phi \cos\theta, \\ v_z &= g_{pre} \sin\phi \sin\theta, \end{aligned}$$

where g_{pre} is the pre-collisional relative velocity, $\cos\phi = 2R_1 - 1$, $\sin\phi = \sqrt{1 - \cos\phi^2}$, $\theta = 2\pi R_2$, and R_1 and R_2 are random numbers.

IV. Results and discussion

Some selected results of the PIC simulation with electron-neutral elastic collisions are presented here. The background neutral densities of 1.0×10^{19} m^{-3}, 1.5×10^{19} m^{-3}, and 2.0×10^{19} m^{-3}, are compared against the baseline case which does not have electron-neutral elastic collisions.

Fig. 1 displays the contour of the azimuthal instantaneous electric field. Fig. 1(a) shows the clear wave structures in azimuthal direction near ionization region due to the ECDI. The transition of the high-frequency, short-wavelength plasma waves to the lower-frequency, large-wavelength plasma waves occurs around $x = 0.75$ cm where the magnetic field is the strongest. In the plume, the lower-frequency plasma wave coexist with the high-frequency plasma wave which stems from the upstream high-frequency wave. In Figs. 1(b) and (c), similar to Fig. 1(a), the high-frequency, short-wavelength ECDI mode dominates in the upstream. It can be seen that the transition to the lower-frequency, large-wavelength mode occurs past the maximum magnetic field location (around $x = 0.8$ cm). In the plume, it can be seen that the short and large wavelength modes coexist, but the amplitude of the electric field for the large-wavelength mode is smaller compared to the no collision case.

In Fig. 1(d), with the higher neutral number density at $n_n = 2.0 \times 10^{19}$ m^{-3}, the ECDI wave does not transition to the large-wavelength mode in the downstream. The wavenumber is roughly the same at the downstream and upstream and is higher than other cases in the plume. The transition to the ion acoustic-like mode is dampened by the presence of electron-neutral collisions. In addition, it can be seen that the amplitude of the wave is significantly weaker than the lower neutral number density cases, indicating that the plasma waves are dampened. Lastly, the formation of the wave structure due to the ECDI near the ionization region in the upstream is quicker, i.e., the growth rate is faster, and the phase velocity of the wave is roughly twice faster in the no collision case compared to the $n_n = 2.0 \times 10^{19}$ m^{-3} case. These results implies the growth rate of the ECDI mode is getting slower as the neutral number density increases.

Fig. 2 shows the axial profiles of the plasma properties. The values are time averaged over 5 μs and azimuthally averaged. In Fig. 2(a), the axial electric field strength are presented. The shift of the peak electric field strength to the downstream and the increase of the peak strength are observed, as the neutral number density increases. The case without collision has the peak at $x = 0.85$ cm while the peaks are located at 0.88, 0.91, 0.97 cm for $n_n = 1.0 \times 10^{19}$ m^{-3}, 1.5×10^{19} m^{-3}, 2.0×10^{19} m^{-3}, respectively. The most remarkable change is for $n_n = 2.0 \times 10^{19}$ m^{-3}. The axial electric field is significantly pushed downstream, resulting in a smaller electric field near the anode (e.g., $x < 0.7$ cm) and large electric field in the near field plume (e.g., 1 cm$< c <$ 1.5 cm) Fig. 2(b) shows the axial profile of the electron number density. Similar to axial electric field, the peak electron number density increases and shifted to the right as the neutral number density increase. In the upstream, the plasma density is large because of low electric field inside the channel, i.e., $x < 1$ cm. In the downstream at $x \geq 1$ cm, the electron number density slightly decreases as oppose to the upstream because the ions are lost more due to the large electric field in the near field

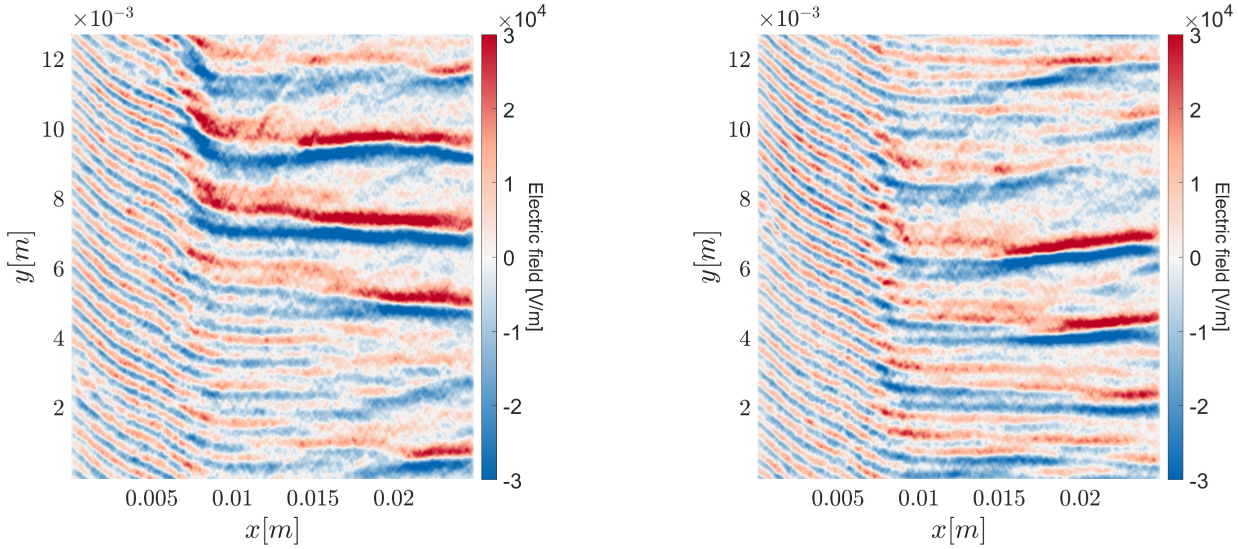

(a) No collisions, i.e., $n_n = 0$ m^{-3}

(b) $n_n = 1.0 \times 10^{19}$ m^{-3}

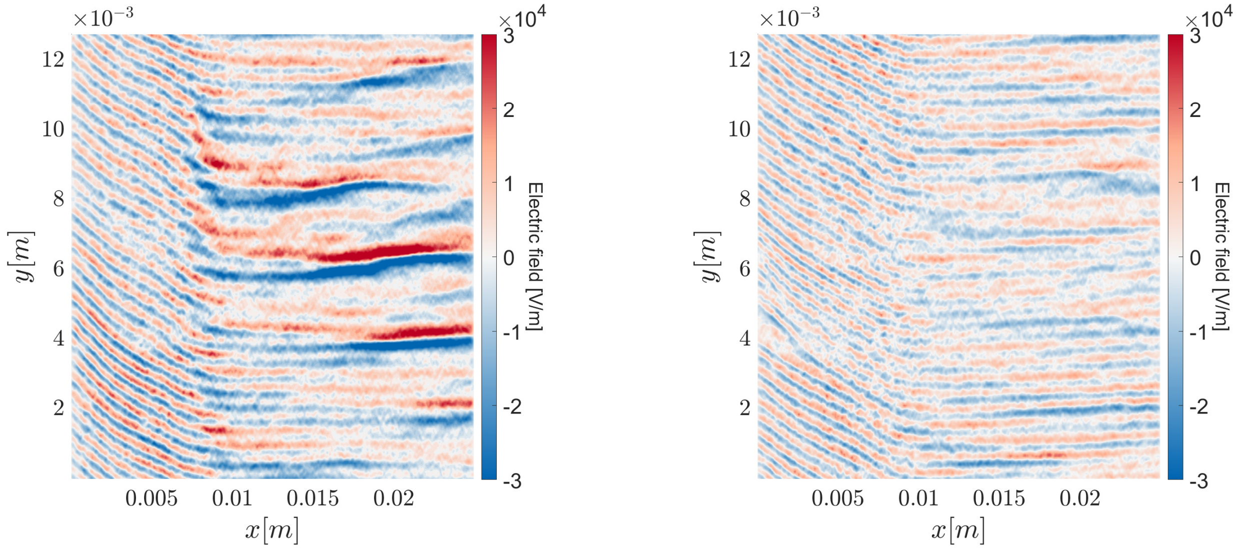

(c) $n_n = 1.5 \times 10^{19}$ m^{-3}

(d) $n_n = 2.0 \times 10^{19}$ m^{-3}

Figure 1: Instantaneous azimuthal electric fields at steady state are shown. The different neutral number density cases are presented.

plume. Fig. 2(c) displays the electron axial bulk velocity profile. Note that the bulk velocity is in $-x$ direction as the electrons travel from downstream to upstream. The magnitude of the electron bulk velocity increases slightly as the neutral number density increases for $n_n = 1.0 \times 10^{19}$ m^{-3} and $n_n = 1.5 \times 10^{19}$ m^{-3}. However, with $n_n = 2.0 \times 10^{19}$ m^{-3}, the electron axial bulk velocity significantly decreases. The increase of the bulk velocity indicates that the electron-neutral collision inducing an enhancement in the cross-field electron transport which is larger than the drag from the collision events. In Fig. 2(d), we can see the electron temperature profile in the axial direction. The peak temperature increases from the no collision case up to $n_n = 1.5 \times 10^{19}$ m^{-3} and starts decreasing with $n_n = 2.0 \times 10^{19}$ m^{-3}. On the other hand, the electron temperature in the downstream, $x \geq 1.5$ cm, monotonically decreases as the neutral number density increases. The location of the peak is monotonically shifted to the right as well. The results can be explained by the heating mechanisms are due to $j \cdot E$ as the heating occurs at downstream.

Cross-field electron mobility profile calculated assuming a drift-diffusion formulation, i.e., Eq. (2), is presented in Fig. 3. The axial mobility of the electron increases as the neutral number density increases up

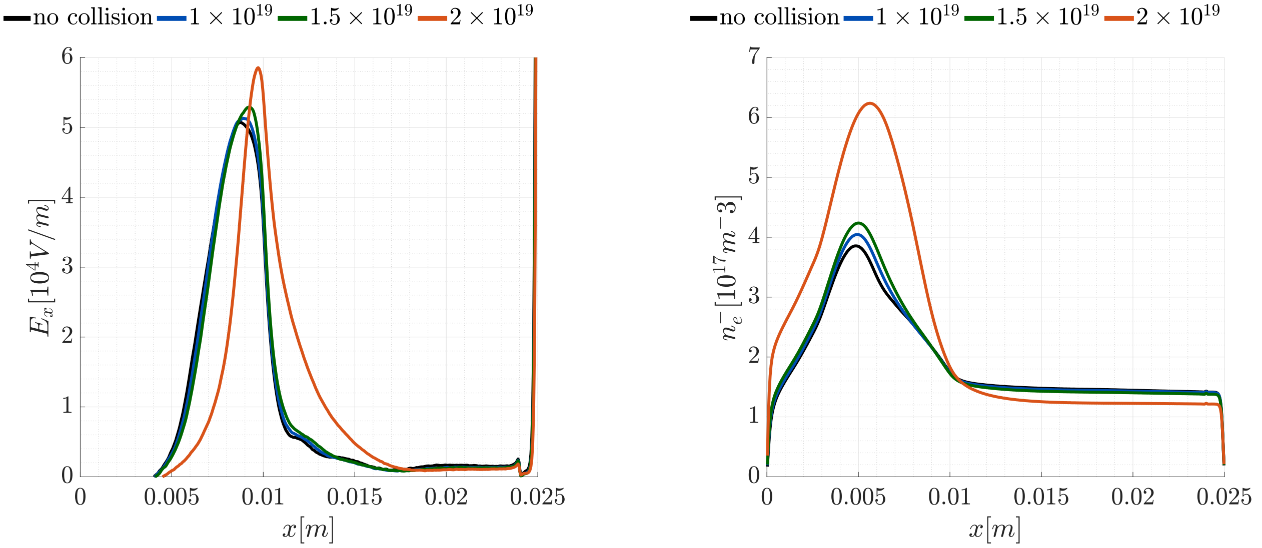

(a) Axial electric field profile.

(b) Electron density profile.

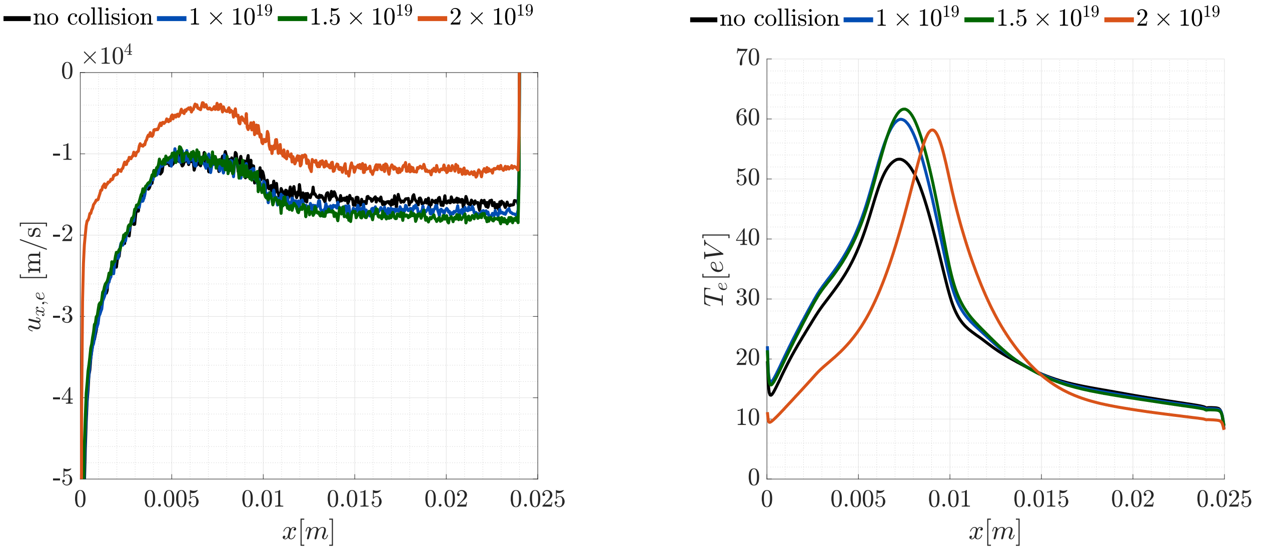

(c) Electron axial bulk density profile.

(d) Electron temperature profile.

Figure 2: Azimuthally and time averaged plasma profile obtained from the PIC simulations. The time average was taken over 5 μs.

to $n_n = 1.5 \times 10^{19}$ m^{-3}. Similar to the electron axial bulk velocity, the axial mobility starts decreasing at $n_n = 2.0 \times 10^{19}$ m^{-3}. Nevertheless, the highest neutral number density cases exceeds the no collision case at the downstream $x \geq 1.8$ cm. This indicates the decrease in the denominator of the Eq. (2) is faster than the decrease in the electron axial bulk velocity as the neutral number density increases.

From a previous study, larger wave energy density stems from the larger amplitude plasma wave and the higher wavenumber in the plume correlate to the higher cross-field electron transport [13]. From Fig. 1, the wavenumber in the plume region increases as the neutral number density increase, but the amplitude of the wave decreases. This trend agrees with the calculated mobility in Fig. 3. $n_n = 1.0 \times 10^{19}$ m^{-3} and $n_n = 1.5 \times 10^{19}$ m^{-3} cases consist of the higher wavenumber and relatively larger amplitude. On the other hand, no collision case has larger amplitude but smaller wavenumber, and $n_n = 2.0 \times 10^{19}$ m^{-3} has high wavenumber but smaller amplitude. Understanding the cause of the wavenumber and amplitude variation is desired as a future path. Previous literature suggest the transition into the short-wavelength mode in the plume is due to the non-magnetized ion-acoustic-type wave [14]. Other literature propose the gradient drift

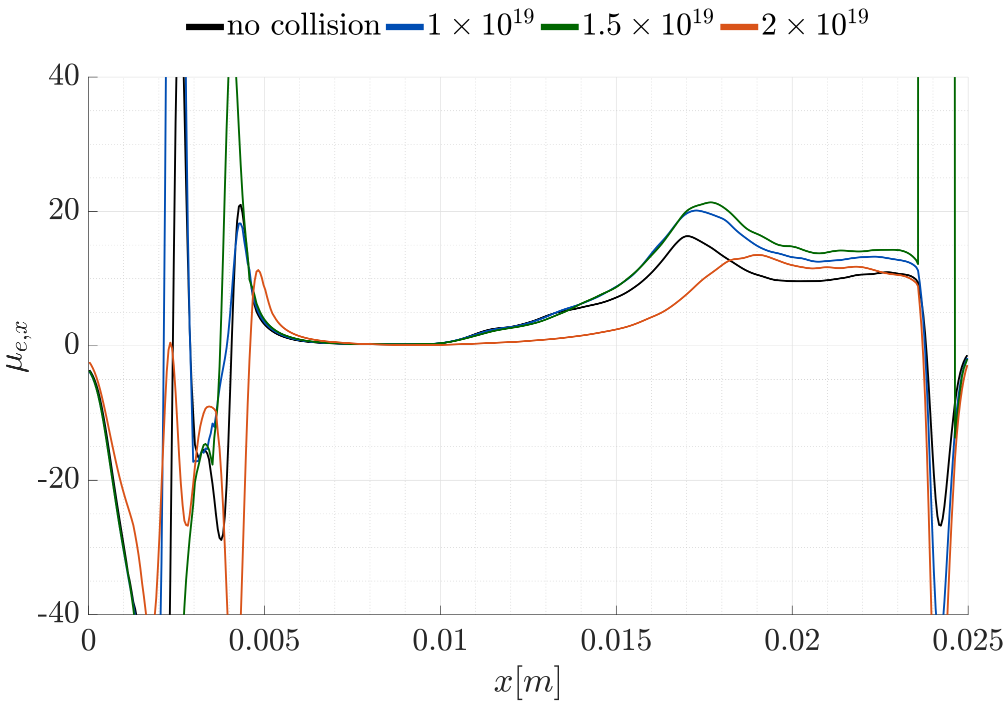

Figure 3: Azimuthally and time averaged axial profile of axial electron mobility for different neutral densities. The time average was taken over 5 μs.

instability as a candidate of the cause [15, 16].

V. Conclusions

In this paper, we present the development and results of 2D axial-azimuthal HET PIC simulation with an electron-neutral elastic MCC model. From the azimuthally and time averaged fluid axial profile, monotonic increase of the electron number density and strength of the axial electric field are recorded. In electron axial bulk velocity, electron temperature, and cross-field electron mobility, increase of the values up to $n_n = 1.5 \times 10^{19}$ m^{-3} are reported. We observed the shift of the axial profile to the cathode side as the neutral number density increases. From no collision base case to $n_n = 1.5 \times 10^{19}$ m^{-3} case, the decrease in the magnitude of both the axial and azimuthal electric field and increase in the wavenumber in the downstream are presented. Moreover, a slight enhancement of the cross-field electron mobility is observed, which can be correlated with the increase in wavenumber of the plasma waves. For the higher neutral density ($n_n = 2.0 \times 10^{19}$ m^{-3}) case, a higher wavenumber plasma wave is observed without transition to the large-wavelength mode. It can be considered that the significant decrease in the wave amplitude in the plume region leads to decrease in the cross-field electron mobility. This study is limited to only ECDI due to abscence of the multiply charged ions which introduce another instability such as the ion-ion two-stream instability. HET PIC simulation with multiply charged species is anticipated to enhance the understanding the effect of the electron-neutral collisions on the cross-field electron transport.

Acknowledgements

This work was supported by NASA through the Joint Advanced Propulsion Institute, a NASA Space Technology Research Institute under Grant No. 80NSSC21K1118. We would like to thank Stanford University and the Stanford Research Computing Center for providing computational resources and support that contributed to these research results.

References

[1] A. I. Morozov. “The conceptual development of stationary plasma thrusters”. In: *Plasma Physics Reports* 29 (Mar. 2003), pp. 235–250.

[2] Jean-Pierre Boeuf and Bhaskar Chaudhury. “Rotating Instability in Low-Temperature Magnetized Plasmas”. In: *Phys. Rev. Lett.* 111 (15 Oct. 2013), p. 155005.

[3] A I Smolyakov et al. “Fluid theory and simulations of instabilities, turbulent transport and coherent structures in partially-magnetized plasmas of $\mathbf{E} \times \mathbf{B}$ discharges”. In: *Plasma Physics and Controlled Fusion* 59.1 (Nov. 2016), p. 014041.

[4] Ioannis G. Mikellides and Ira Katz. “Numerical simulations of Hall-effect plasma accelerators on a magnetic-field-aligned mesh”. In: *Phys. Rev. E* 86 (4 Oct. 2012), p. 046703.

[5] Kentaro Hara. “An overview of discharge plasma modeling for Hall effect thrusters”. In: *Plasma Sources Science and Technology* 28.4 (Apr. 2019), p. 044001.

[6] T Charoy et al. “2D axial-azimuthal particle-in-cell benchmark for low-temperature partially magnetized plasmas”. In: *Plasma Sources Science and Technology* 28.10 (Oct. 2019), p. 105010.

[7] J. C. Adam, A. Héron, and G. Laval. “Study of stationary plasma thrusters using two-dimensional fully kinetic simulations”. In: *Physics of Plasmas* 11.1 (Jan. 2004), pp. 295–305.

[8] A. Héron and J. C. Adam. “Anomalous conductivity in Hall thrusters: Effects of the non-linear coupling of the electron-cyclotron drift instability with secondary electron emission of the walls”. In: *Physics of Plasmas* 20.8 (Aug. 2013), p. 082313.

[9] Kentaro Hara and Sedina Tsikata. “Cross-field electron diffusion due to the coupling of drift-driven microinstabilities”. In: *Phys. Rev. E* 102 (2 Aug. 2020), p. 023202.

[10] J. Cavalier et al. “Hall thruster plasma fluctuations identified as the E×B electron drift instability: Modeling and fitting on experimental data”. In: *Physics of Plasmas* 20.8 (Aug. 2013), p. 082107.

[11] T. Lafleur, Scott Baalrud, and Pascal Chabert. “Theory for the anomalous electron transport in Hall effect thrusters. II. Kinetic model”. In: *Physics of Plasmas* 23 (May 2016), p. 053503.

[12] P. Kumar, S. Tsikata, and K. Hara. “Effects of multiply charged ions on microturbulence-driven electron transport in partially magnetized plasmas”. In: *Journal of Applied Physics* 130.17 (Nov. 2021), p. 173307.

[13] Sean T. Sewell, Prabhat Kumar, and Kentaro Hara. “Effects of the Wavelength of the Plasma Waves on Cross-Field Electron Transport in Partially Magnetized Plasmas”. In: *IEEE Transactions on Plasma Science* 50.10 (2022), pp. 3498–3506.

[14] Jean-Pierre Boeuf and Laurent Garrigues. “E × B electron drift instability in Hall thrusters: Particle-in-cell simulations vs. theory”. In: *Physics of Plasmas* 25 (June 2018), p. 061204.

[15] Y. Sakawa et al. “Excitation of the modified Simon–Hoh instability in an electron beam produced plasma”. In: *Physics of Fluids B: Plasma Physics* 5.6 (June 1993), pp. 1681–1694.

[16] Kentaro Hara, Adnan R. Mansour, and Sedina Tsikata. “Theory of gradient drift instabilities in low-temperature, partially magnetised plasmas”. In: *Journal of Plasma Physics* 88.4 (2022), p. 905880408.